

A MULTI-STAGE BAYESIAN PREDICTION FRAMEWORK FOR SUBSURFACE FLOWS

V. Ginting,¹ F. Pereira,^{2,*} & A. Rahunanthan³

¹Department of Mathematics, University of Wyoming, Laramie, WY 82071, USA

²Departments of Chemical and Petroleum Engineering and Mathematics, School of Energy Resources, University of Wyoming, Laramie, WY 82071, USA

³Department of Mathematics and Computer Science, Edinboro University, Edinboro, PA 16444, USA

Original Manuscript Submitted: 04/28/2012; Final Draft Received: 12/14/2012

We are concerned with the development of computationally efficient procedures for subsurface flow prediction that relies on the characterization of subsurface formations given static (measured permeability and porosity at well locations) and dynamic (measured produced fluid properties at well locations) data. We describe a predictive procedure in a Bayesian framework, which uses a single-phase flow model for characterization aiming at making prediction for a two-phase flow model. The quality of the characterization of the underlying formations is accessed through the prediction of future fluid flow production.

KEY WORDS: Bayesian statistics, GPUs, Markov chain Monte Carlo, single-phase, two-phase, uncertainty quantification

1. INTRODUCTION

It is generally accepted that permeability and porosity are two of the most important subsurface properties governing the movement and storage of the fluids. Mainly because the variation in porosity is typically at least one order of magnitude smaller than the variation in permeability, it has been a routine assumption to take the porosity as a deterministic constant in predictive simulations. Alternatively, others (see for example [1, 2]) have investigated possible correlations between permeability and porosity, but these are largely empirical in nature and were developed on a case-by-case basis. Characterization of both permeability and porosity fields is a practical way of reducing the uncertainty in the whole flow and transport pattern of the subsurface [3]. In general, the characterization is realized through iteratively adjusting the subsurface model until it closely reproduces the available recorded dynamic and static data [4–7]. A set of governing mathematical equations and the corresponding numerical simulations are imperative for making the comparison possible. These equations involve several unknown functions, such as pressure, velocity, and saturation, and are spatially and time dependent. Furthermore, the interactions between these unknowns are modeled by nonlinear coupling appearing in the constitutive relations.

A commonly used procedure for characterizing the subsurface is *tracer testing* (see for example [3, 8–14]). In this procedure, one or more tracers, such as chemical or radioactive compounds, are injected into the subsurface in order to estimate its flow pattern and storage. The tracer test data in the form of amount of produced fluids are recorded, which is the basis for testing the validity of proposed permeability and porosity fields. It is then followed by numerical test simulation with exact injection and extraction operations, tracer details, and boundary conditions, etc., of the experimental setup and history matching of the simulated response with the available data at the extraction wells. In this respect, tracer testing offers an appealing feature since its numerical simulation is relatively inexpensive

*Correspond to F. Pereira, E-mail: lpereira@uwoyo.edu

in comparison to the nonlinear case. Specifically, solving the Darcy velocity, which considerably is the most expensive component, occurs only one time, after which it is proceeded by solving the transport equation.

Within the statistical framework, the above subsurface characterization can be thought of as sampling the parameters from a probability distribution that is conditioned to the available output data. The spatially dependent nature of the parameters makes them belong to an infinite dimensional space, which up to some numerical discretization can be approximated by some finite-dimensional space. However, this dimension by far exceeds the dimension of the space of the guiding measurement data. It is not surprising that a successful match between simulated and measured data does not necessarily guarantee obtaining the exact parameters of the subsurface, thus making the characterization an ill-posed mathematical problem in the sense that we attempt to invert a higher dimensional map whose range has a much lower dimension.

As mentioned, even at the discretized level, the dimension of the uncertainty space may be exceptionally large, so reduction-of-order techniques are needed to bring down the whole calculation to the extent that it becomes amenable for computational simulations. This can be achieved by the Karhunen–Loève expansion, which allows for parametrization of the uncertainty space. The characterization is undertaken by sampling the parametric variables in the expansion. Still, a practical way of inverting the system in the characterization needs to be elaborated properly. An alternative to direct inversion of the system is to use implicit inverse models in a Bayesian approach to estimate permeability and porosity of the subsurface. These parameter estimates are updated automatically in a Markov chain Monte Carlo Method (MCMC) in response to computed sensitivity of simulated data to changes in these parameters.

Many authors studied Bayesian methods for inverse problems in reservoir modeling. We refer the reader to [15, 16] for recent works in the study of inverse problems in applications of flow through porous media. In [15], the authors used an intrinsically stationary Markov random field, which compares favorably to Gaussian process models and offers some additional flexibility and computational advantages for the choice of prior for the unknown permeability field. Through a Bayesian approach, using MCMC methods to explore the high-dimensional posterior distribution, they investigated the characterization of an aquifer based on flow data. In contrast, [17–19] used the Karhunen–Loève expansion [20] to parametrize the permeability field.

In practice however, MCMC can be computationally expensive, particularly for solving forward problems in significantly correct fine grids in real flow problems. A methodology for improving the speed and efficiency of an MCMC analysis by combining runs on different scales is presented in [21]. In their approach, by using a coarser scale, the MCMC chain can run faster and better explore the posterior, being less likely to become stuck in local maxima. They discussed methods for linking the coarse chain back to the original fine-scale chain of interest. The proposed coupled MCMC runs more efficiently without sacrificing the accuracy achieved at the finer scale. In [17, 19], a two-stage MCMC that utilizes inexpensive coarse-scale models to screen out detailed flow and transport simulations was used to explore the posterior distribution of permeability field. In the first stage, a new proposal is first tested at the coarse-scale model. If the proposal passes the testing at the coarse-scale model, then at the second stage the fine-scale simulation will be run and this fine-scale run is very expensive compared to the coarse-scale run. We remark that this procedure is closely related to the method proposed in [22, 23].

In this paper, we present a multi-stage Bayesian prediction framework for subsurface flows. To the best of our knowledge, integration of single- and two-phase models into a predictive simulation has not been reported in the existing literature. The technique constitutes two steps, namely (1) a subsurface characterization step employing Bayesian MCMC whose “black-box” is the tracer testing, which is governed by a single-phase flow model, and (2) a prediction step in which the resulting subsurface characterization is used as an input in multi-phase flow model. Our final aim in this case is to predict the entire production curves for multi-phase flows in subsurface. Instead of assuming ad-hoc correlations between permeability and porosity fields, we model these fields as independent random fields. The authors presented a preliminary study of this work in [24].

The main attractive feature of this technique lies in the efficiency of the characterization. As pointed out, the MCMC calculation is expensive because whenever a sample of parameters is proposed, it has to be sent to the black box to get the simulated response, which in turn is compared to the measured data. The whole MCMC can easily require thousands of iterations before a steady state distribution is reached. Hence using a relatively simple physics (and thus is easy to solve) in the black box is preferable due to efficiency consideration. The tracer testing model is a very good candidate for this purpose. On the other hand, once the accepted parameters samples have been collected,

they can be used solely for prediction. In this case, a more representative model is used, such as the multi-phase flow model, that better reflects the actual physics of the flow and transport. Obviously, solving this model will be more challenging, but one can manage to do this because the number of accepted samples to be used as input in it is at most the fraction of the original MCMC iterations. The second step in the proposed technique can be thought of as a postprocessing in which a standard Monte Carlo simulation is carried out to gather statistics of the quantities of interest in the prediction.

We use a Metropolis–Hastings MCMC with a random walk sampler to explore the posterior distribution. Since we explore high-dimensional posterior distribution, we implement a component-wise tuning mechanism in the two-stage MCMC. Owing to the computational burden in the MCMC sampling, we parallelize the numerical algorithms for solving the forward problem. Recent investigation on the use of a GPU for solving multi-phase flow problems in a three-dimensional setting indicates a speed-up of up to 60 in comparison to the traditional serial calculation on a CPU [25]. In the current work we exploit the advances in GPU computing by using a heterogeneous CPU–GPU system to solve the forward problems.

We assume that we have the values of permeability and porosity at the wells, and the recorded tracer test data of the subsurface in the form of fraction of tracer in the produced fluid–fractional flow curve at the extraction wells. Due to economic considerations, a tracer test is frequently terminated before the tracer concentrations fall below the detection limit. Therefore, we use partial fractional flow curves of the extraction wells and characterize the permeability and porosity fields of the subsurface using the Karhunen–Loève expansion with a two-stage MCMC method. Based on the characterization of the fields, we then run the forward problem in a two-phase flow model for the accepted realizations and predict the entire production curves of the two-phase flow problem by aggregating the solutions of the forward problem. Here the single- and two-phase forward models are solved on the same underlying field. For given partial tracer curves, there exist many different distributions of permeability and porosity. We consider most of such distributions through the MCMC and accurately predict an integrated response for such distributions in the two-phase model. Numerical results indicate that the predictions are reliable, in particular our proposed technique predicts the breakthrough times very accurately.

This paper is organized as follows. We discuss physical modeling of the problem in Section 2. In Section 3, numerical models and associated methods are discussed. In Section 4, spatial priors for unknown permeability and porosity fields are specified using the Karhunen–Loève expansion. In Section 5, we discuss a Bayesian approach for sampling both permeability and porosity fields using a two-stage MCMC method. In Section 6, numerical experiments are presented to demonstrate the performance of the approach for characterizing subsurfaces and predicting the fractional flow curves. Section 7 contains our conclusions.

2. PHYSICAL MODELING

We consider a heterogeneous oil reservoir that is confined in a domain $\Omega \subset \mathbf{R}^2$. The reservoir is equipped with an injection well, from which water is discharged to displace the trapped oil towards the production wells, situated on the perimeter of the domain (see Fig. 1). The dynamics of the movement of the fluids in the reservoir is categorized as an

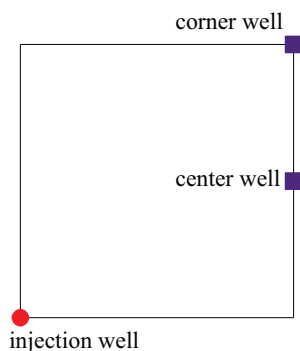


FIG. 1: The description of the problem. The injection and extraction (or production) wells are on the perimeter.

immiscible two-phase system with water and oil (denoted by w and o , respectively) that is incompressible. Capillary pressure is not included in the model. Further simplifying assumptions that we use are a gravity-free environment with no sources or sinks (injection and production are modeled through boundary conditions), the two fluids fill the pore space and rigid porous media. Then, the Darcy's law with a statement of conservation of mass allow us to write the governing equations of the flow as

$$\nabla \cdot \mathbf{v} = 0, \quad \text{where } \mathbf{v} = -\lambda(s)k(\mathbf{x})\nabla p, \quad (1)$$

and

$$\phi(\mathbf{x}) \frac{\partial s}{\partial t} + \nabla \cdot (f(s)\mathbf{v}) = 0, \quad (2)$$

where \mathbf{v} is the total Darcy velocity ($\mathbf{v}_w + \mathbf{v}_o$), \mathbf{v}_j , $j = w, o$ is the phase velocity, s is the water saturation, k is the permeability, and ϕ is the porosity. The total mobility $\lambda(s)$ and the flux function $f(s)$ are respectively given by

$$\lambda(s) = \frac{k_{rw}}{\mu_w} + \frac{k_{ro}}{\mu_o}, \quad f(s) = \frac{k_{rw}(s)/\mu_w}{\lambda(s)}, \quad (3)$$

where k_{rj} , $j = w, o$, is the relative permeability of the phase j [26]. In the numerical implementation, all the wells are modeled through appropriate boundary conditions. More specifically, we use the boundary conditions $\mathbf{v} \cdot \mathbf{n} = g_N$ on the Neumann boundary Γ_N and $p = 0$ on the Dirichlet boundary Γ_D , with $\Gamma_N \cup \Gamma_D = \partial\Omega$ for a given flux g_N .

Sampling the permeability and porosity of the reservoir employs the tracer testing, which is governed by the single-phase flow model, represented by (1) and (2), with $\lambda(s) = 1$ and $f(s) = s$, where s is the concentration of the tracer in the fluid. The tracer test data serving as the guiding measurement are modeled by the partial fractional curves. For each production boundary the fractional flow $F(t)$ is defined as the fraction of tracer chemical in the produced fluid, i.e.,

$$F(t) = 1 - \frac{\int_{\partial\Omega_{\text{out}}} v_n f(s) dl}{\int_{\partial\Omega_{\text{out}}} v_n dl}, \quad (4)$$

where $\partial\Omega_{\text{out}}$ denotes outflow boundary, v_n is normal velocity field, and t in dimensionless time PVI, which is computed as

$$\text{PVI} = \int_0^T V_p^{-1} \int_{\partial\Omega_{\text{out}}} v_n dl d\tau, \quad (5)$$

where V_p is the total pore-volume of the reservoir and T denotes the time taken for injection of water.

3. NUMERICAL MODELING

At the core of the numerical approximation is the partition of Ω into non-overlapping rectangular elements of $I_{i,j}$. Let $x_i := 0.5(2i-1)h_x$, $y_j := 0.5(2j-1)h_y$, $x_{i\pm 1/2} := x_i \pm 0.5h_x$ and $y_{j\pm 1/2} := y_j \pm 0.5h_y$, where $i = 1, \dots, N$ and $j = 1, \dots, M$ with N and M denote the number of elements in x - and y -direction, respectively, and h_x and h_y denote the sizes of the element in x - and y -direction, respectively. We then define $I_{i,j} := [x_{i-1/2}, x_{i+1/2}] \times [y_{j-1/2}, y_{j+1/2}]$.

To solve the models, we employ an operator splitting technique to compute the solutions of the pressure equation (1) and saturation (2), which are coupled together by the Darcy velocity \mathbf{v} and water saturation s . Typically, computational efficiency dictates the use of larger time steps to compute the pressure equation (1). The splitting technique allows time steps used in the pressure calculation that are longer than the steps allowed under an appropriate CFL condition in the saturation calculation. We thus introduce a variable time step Δt_s for the saturation calculation, and a longer time step Δt_p for the pressure calculation. The pressure and the Darcy velocity are approximated at times $t^m = m\Delta t_p$, where $m = 0, 1, \dots$; the saturation is approximated at times $t^{m,k} = t^m + \sum_{i=1}^k (\Delta t_s)_i$ for $t^m < t^{m,k} \leq t^{m+1}$. Here, we need to specify the water saturation at $t = 0$. For further details on the operator splitting procedure, we refer the reader to [27–29]. We remark that one could also take advantage of the linearity of the transport equation in the single-phase model by using accurate, Lagrangian solution methods that do not have restrictions on the time step size (see, e.g., [30]).

In the simulation of (1) and (2), maintaining the divergence-free property of the Darcy velocity is very important. This is precisely the reason for employing a mixed finite element method to solve (1). To this end, let $\mathbf{U}_g = \{\mathbf{v} \in \mathbf{H}(\text{div}, \Omega) : \mathbf{v} \cdot \mathbf{n}|_{\Gamma_N} = g\}$ and we set $\mathbf{U}_{h,g} \subset \mathbf{U}_g$ and $\mathbf{W}_h \subset L^2(\Omega)$ to be the lowest-order Raviart–Thomas spaces [31] over rectangles. The mixed finite element approximation (1) consists of finding $(\mathbf{v}_h, p_h) \in \mathbf{U}_{h,g_N} \times \mathbf{W}_h$ such that

$$\begin{aligned} (\lambda^{-1}(s_h)k^{-1}(\mathbf{x})\mathbf{v}_h, \mathbf{u}) - (p_h, \nabla \cdot \mathbf{u}) &= 0, \quad \forall \mathbf{u} \in \mathbf{U}_{h,0}, \\ (\nabla \cdot \mathbf{v}_h, w) &= 0, \quad \forall w \in \mathbf{W}_h. \end{aligned} \quad (6)$$

The resulting algebraic system is then efficiently solved in a GPU by the conjugate gradient method preconditioned by the algebraic multi-grid scheme [32]. The approximate pressure p_h is computed at the center of each cell $I_{i,j}$ while the velocity \mathbf{v}_h is computed at the four edges of the cell $I_{i,j}$.

To solve (2), we use a conservative second-order, high-resolution central scheme, which can be viewed as a generalization of Kurganov–Tadmor central scheme [33]. Our version of the Kurganov–Tadmor scheme for the case of variable porosity fields is described in detail in Appendix A for conservation laws in one space dimension. The design and implementation of a multi-dimensional version of this scheme is outside the scope of the work presented here and will appear elsewhere. We refer the reader to [25, 34] for further discussion on the numerical schemes used in solving the forward problem possibly taking advantage of GPU computing.

4. PARAMETRIZATION OF UNCERTAINTY

As the uncertainty space describing the permeability and porosity can be exceptionally large, a reduction of the space dimension is a step that must be performed for computationally feasible simulations. The Karhunen–Loève (KL) expansion [20, 35] allows for the parametrization of the uncertainty space and thereby leads to the desired reduction. We note that this reduction technique has been applied within Bayesian MCMC in [16–19, 36].

The KL expansion relies on a basic prior information on the structure of the permeability and porosity fields that reasonably match the actual reservoir. In practice, however, this is hindered by the very limited information available to use. A standard assumption in geostatistics is to model the permeability to follow a log-normal distribution [37], i.e., $\log[k(\mathbf{x}, \omega)] = Y^k(\mathbf{x}, \omega)$, where $\mathbf{x} \in \Omega \subset \mathbf{R}^2$, and ω is a random element in a probability space, and $Y^k(\mathbf{x}, \omega)$ is a field possessing a Gaussian distribution and a covariance function

$$R(\mathbf{x}_1, \mathbf{x}_2) = \sigma_Y^2 \exp\left(-\frac{1}{2}|\mathbf{L}^{-1}(\mathbf{x}_1 - \mathbf{x}_2)|^2\right), \quad (7)$$

where, $\mathbf{L} = [L_x \ L_y]$ with $L_x = [L_{xx} \ L_{yx}]^\top$ and $L_y = [L_{xy} \ L_{yy}]^\top$ with the correlation lengths L_{ij} , where i and j denote x - and y -direction, respectively.

We now briefly describe the essentials of the KL expansion. Suppose $Y^k(\mathbf{x}, \omega)$ is a second-order stochastic process, that is, $Y^k(\mathbf{x}, \omega) \in L^2(\Omega)$ with a probability of one. We will assume that $E[Y^k(\mathbf{x}, \omega)] = 0$. Given an arbitrary orthonormal basis $\{\varphi_i\}$ in L^2 , we can expand $Y^k(\mathbf{x}, \omega)$ as

$$Y^k(\mathbf{x}, \omega) = \sum_{i=1}^{\infty} Y_i^k(\omega) \varphi_i(\mathbf{x}), \quad \text{with} \quad Y_i^k(\omega) = \int_{\Omega} Y^k(\mathbf{x}, \omega) \varphi_i(\mathbf{x}) d\mathbf{x} \quad (8)$$

being functions of a random variable. We are interested in the special basis in $L^2(\Omega)$ that allows Y_i^k to be uncorrelated, $E[Y_i^k Y_j^k] = 0$ for all $i \neq j$. Because by definition $R(\mathbf{x}_1, \mathbf{x}_2) = E[Y^k(\mathbf{x}_1) Y^k(\mathbf{x}_2)]$, such basis functions $\{\varphi_i\}$ satisfy

$$E[Y_i^k Y_j^k] = \int_{\Omega} \varphi_i(\mathbf{x}_1) d\mathbf{x}_1 \int_{\Omega} R(\mathbf{x}_1, \mathbf{x}_2) \varphi_j(\mathbf{x}_2) d\mathbf{x}_2 = 0, \quad i \neq j. \quad (9)$$

Completeness of $L^2(\Omega)$ implies that $\varphi_i(\mathbf{x})$ is an eigenfunction of integral equation involving $R(\mathbf{x}_1, \mathbf{x}_2)$ expressed as

$$\int_{\Omega} R(\mathbf{x}_1, \mathbf{x}_2) \varphi_i(\mathbf{x}_2) d\mathbf{x}_2 = \lambda_i \varphi_i(\mathbf{x}_1), \quad i = 1, 2, \dots \quad (10)$$

where $\lambda_i = E[(Y_i^k)^2] > 0$. Denoting $\theta_i^k = Y_i^k / \sqrt{\lambda_i}$, then θ_i^k satisfies $E(\theta_i^k) = 0$ and $E(\theta_i^k \theta_j^k) = \delta_{ij}$, and thus

$$Y^k(\mathbf{x}, \omega) = \sum_{i=1}^{\infty} \sqrt{\lambda_i} \theta_i^k(\omega) \varphi_i(\mathbf{x}), \quad (11)$$

where φ_i and λ_i satisfy (10). We assume that eigenvalues λ_i are ordered so that $\lambda_1 \geq \lambda_2 \geq \dots$. The expansion (11) is called the Karhunen–Loève expansion. In (10), the L^2 basis functions $\varphi_i(\mathbf{x})$ are deterministic and resolve the spatial dependence of the permeability field. The uncertainty is represented by the scalar random variables θ_i^k . In general, we need to keep only the leading order terms (quantified by the magnitude of λ_i) and still capture most of the energy of the stochastic process $Y^k(\mathbf{x}, \omega)$. For a N_k -term KL expansion

$$Y_{N_k}^k = \sum_{i=1}^{N_k} \sqrt{\lambda_i} \theta_i^k \varphi_i. \quad (12)$$

If λ_i decays very fast, then the truncated KL expansion would be a good approximation of the stochastic process in the L^2 sense.

We remark that one could use a different covariance function, such as for example,

$$R(\mathbf{x}_1, \mathbf{x}_2) = \sigma_Y^2 \exp \left(-\frac{|x_1 - x_2|}{L_x} - \frac{|y_1 - y_2|}{L_y} \right). \quad (13)$$

However, the eigenvalues of KL expansion may decay algebraically [17, 38]. To have a good approximation for (11), we must add more terms in the truncated KL expansion (12). This will increase the parameter space dimension, and thus make the sampling of permeability and porosity more expensive.

We first solve the eigenvalue problem (10) numerically [typically in coarser grids than those used for the approximation of the (1) and (2)], and obtain the eigenpairs (λ_i, φ_i) . Hence, the truncated KL expansion should approximate the stochastic process $Y^k(\mathbf{x}, \omega)$ fairly well. Therefore, we can sample $Y^k(\mathbf{x}, \omega)$ from the truncated KL expansion (12) by generating Gaussian random variables θ_i^k .

Moreover, suppose the permeability field is known at n_w locations. Then, we can incorporate these permeability values in the KL expansion by setting

$$\sum_{i=1}^{N_k} \sqrt{\lambda_i} \theta_i^k \varphi_i(\mathbf{x}_j) = w_j, \quad (14)$$

where w_j are constants that correspond to known permeabilities at locations \mathbf{x}_j , where $j = 1, \dots, n_w$. Now, we propose $(N_k - n_w)$ θ 's and compute the rest of n_w θ 's by solving the linear system (14).

With respect to the porosity field, we make use of the standard assumption that the porosity exhibits a similar spatial correlation structure to the permeability. In turn, this allows us to employ the Karhunen–Loève basis functions (10). As in the KL expansion for the permeability field, we use a N_ϕ -term KL expansion

$$Y_{N_\phi}^\phi(\mathbf{x}, \omega) = \sum_{i=1}^{N_\phi} \sqrt{\lambda_i} \theta_i^\phi(\omega) \varphi_i(\mathbf{x}). \quad (15)$$

Then we define the porosity as

$$\phi(\mathbf{x}) = \frac{\phi_{\min} + \phi_{\max} e^{Y_{N_\phi}^\phi}}{1 + e^{Y_{N_\phi}^\phi}}, \quad \phi_{\min} \text{ and } \phi_{\max} \in (0, 1), \quad (16)$$

where ϕ_{\min} and ϕ_{\max} are the deterministic lower and upper limits of the porosity of the reservoir. This definition ensures that the porosity not only shares the same correlation structure with the permeability, but also falls between ϕ_{\min} and ϕ_{\max} .

5. A TWO-STAGE BAYESIAN MCMC

As alluded to earlier, we want to sample the permeability and porosity fields conditioned on the available fractional flow data F_m . This is translated into sampling from the conditional distribution $P(\boldsymbol{\Psi}|F_m)$, where $\boldsymbol{\Psi} = [\boldsymbol{\theta}^k \ \boldsymbol{\theta}^\phi]$ with $\boldsymbol{\theta}^k$ and $\boldsymbol{\theta}^\phi$ vectors containing the random coefficients in the KL expansions. According to Bayes' theorem this distribution satisfies the proportionality relation

$$P(\boldsymbol{\Psi}|F_m) \propto P(F_m|\boldsymbol{\Psi})P(\boldsymbol{\Psi}), \quad (17)$$

where $P(F_m|\boldsymbol{\Psi})$ represents the likelihood function (which requires the forward solution of the single-phase flow) and $P(\boldsymbol{\Psi})$ is the prior distribution of $\boldsymbol{\Psi}$. The normalizing constant in this expression is not important, because we use an iterative updating procedure. Although a more general error model can be used in the simulations, we assume that the likelihood function follows a Gaussian distribution, i.e.,

$$P(F_m|\boldsymbol{\Psi}) \propto \exp\left(- (F_m - F_\Psi)^\top \Sigma (F_m - F_\Psi)\right), \quad (18)$$

where F_Ψ is the simulated fractional flow curve that is obtained by solving the forward problem with known permeability k and porosity ϕ , in other words with known $\boldsymbol{\Psi}$, and Σ is the covariance matrix representing the measurement errors. We take $\Sigma = \mathbf{I}/2\sigma_F^2$, where \mathbf{I} is the identity matrix and σ_F^2 is the precision associated with the measurement F_m and numerical solution F_Ψ [17, 19].

We use the Metropolis–Hasting MCMC to sample from the posterior distribution. At each iteration, $\boldsymbol{\Psi}_p = [\boldsymbol{\theta}_p^k \ \boldsymbol{\theta}_p^\phi]$ is proposed using an instrumental distribution $q(\boldsymbol{\Psi}_p|\boldsymbol{\Psi})$, where $\boldsymbol{\Psi}$ represents the previously accepted state/parameters in the chain, and then the forward problem is solved to determine the acceptance probability,

$$\alpha(\boldsymbol{\Psi}, \boldsymbol{\Psi}_p) = \min\left(1, \frac{q(\boldsymbol{\Psi}|\boldsymbol{\Psi}_p)P(\boldsymbol{\Psi}_p|F_m)}{q(\boldsymbol{\Psi}_p|\boldsymbol{\Psi})P(\boldsymbol{\Psi}|F_m)}\right), \quad (19)$$

i.e., $\boldsymbol{\Psi}_p$ is accepted with probability $\alpha(\boldsymbol{\Psi}, \boldsymbol{\Psi}_p)$.

In most reservoir simulations, solving the fine-scale forward problem is computationally expensive. Thus, the single-stage MCMC limits the exploration of the posterior in a practical time. Therefore, we use a coarse-scale solution based on upscaling before running the fine-scale flow simulator. Here, we run the flow simulator on the coarse-scale model and compare the fractional flow curves to determine if we need to run on the fine-scale model.

We now briefly describe the two-stage MCMC discussed in [17, 19]. In the two-stage MCMC a screening process is implemented using a coarse-scale model approximating the original equations (1) and (2). First, we proceed by giving a brief description of this coarse-scale model. It is solved on a coarse grid whose discretization is done in a similar fashion as in the fine-scale calculation described in Section 3, but with discretization parameters significantly larger than their fine-scale counterpart. The key lies on a rigorous representation of k and ϕ on the coarse grid obtained from the fine-grid resolution. In this case, we use an upscaling procedure such that effective permeability and porosity fields on the coarse grid deliver the same spatial average response as that of the underlying fine-scale problem locally.

To compute the effective permeability on the coarse grid, we solve for ζ governed by equations similar to (1) subject to the constant pressure and no flux boundary conditions on each coarse-grid cell \bar{I} . After solving these equations on the coarse grid, we compute the effective permeability tensor as [39]

$$(\bar{k}(\mathbf{x})e_i, e_j) = \frac{1}{|\bar{I}|} \int_{\bar{I}} (k(\mathbf{x})\nabla\zeta_i(\mathbf{x}), e_j) d\mathbf{x}, \quad (20)$$

where e_i is the standard Euclidean basis vector. Once we know the effective permeability on the coarse-grid cells, we can solve (1) on the coarse grid with \bar{k} replacing k to get the upscaled Darcy velocity. We compute the effective porosity $\bar{\phi}$ as the arithmetic average over each \bar{I} , i.e.,

$$\bar{\phi} = \frac{\sum_{i=1}^N \phi_i}{N} \quad (21)$$

where N is the number of fine-grid elements in \bar{I} and ϕ_i denotes the porosity value of i th fine-grid element in \bar{I} . In a similar fashion, we solve (2) on the coarse grid with the effective porosity. In Fig. 2 it is not difficult to see that the numerical solution of the coarse-scale model on the grid of 16×16 is relatively inexpensive compared to the calculation on the fine grid of 128×128 and yet it manages to capture the general trend of the process. Hence it is suitable for the screening purpose mentioned above.

Algorithm 1. Two-Stage MCMC

Given the covariance function R , generate KLE parametrization $\{\lambda_n, \varphi_n\}_{n=1}^N$

for $p = 1$ to M_{mcmc} **do**

(1) At $\psi = (\theta^k, \theta^\phi)$, generate $\psi_p = (\theta_p^k, \theta_p^\phi)$ from $q(\psi_p|\psi)$

(2) With ψ_p , compute upscaled \bar{k} and $\bar{\phi}$ on the coarse grid using KLE on the fine grid and solve the forward problem on the coarse grid to get F_c

(3) Accept ψ_p with probability

$$\alpha_c(\psi, \psi_p) = \min \left(1, \frac{q(\psi|\psi_p)P_c(\psi_p|F_m)}{q(\psi_p|\psi)P_c(\psi|F_m)} \right)$$

(4) If ψ_p is rejected, go back to (1), else use ψ_p in the fine-grid simulation to get F_f

(5) Take ψ_p with probability

$$\alpha_f(\psi, \psi_p) = \min \left(1, \frac{P_f(\psi_p|F_m)P_c(\psi|F_m)}{P_f(\psi|F_m)P_c(\psi_p|F_m)} \right)$$

end

The basic procedure of the two-stage MCMC is shown in the Algorithm. Since we explore the high-dimensional posterior distribution, we use a component-wise tuning mechanism in the MCMC. We consider the random walk sampler, $\theta_p^L = \theta^L + \delta^L \epsilon$, where L represents k or ϕ , θ^L is the previously accepted proposal, θ_p^L is the current proposal, δ^L is the tuning parameter, and ϵ is a set of Gaussian random variables. Here, we treat θ^k and θ^ϕ separately. We need to find δ^L such that the MCMC chain has a good acceptance rate and converges fast. We run the chain for few iterations and find the acceptance rate. We reduce the step sizes if the acceptance rate is too low, or increase it if the chain is moving very slowly (i.e., tune δ^L so that the sampler has an acceptance rate that is neither too high nor too low). In our simulations the value of each component of δ^L is set to 1.0 targeting an acceptance rate of about

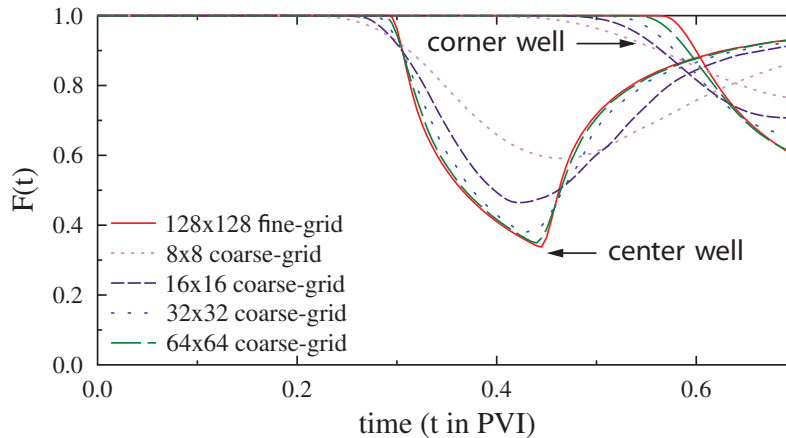


FIG. 2: A comparison of simulated fractional flow obtained from upscaled model and fine-scale model.

40%. In practice, to balance MCMC algorithm acceptance rates and size of steps through the posterior distribution of the parameter space, we sample sub-vectors (or components) of θ^L , which means we are faced with evaluating the likelihood and running the simulator for each sub-vector (or component) of θ^L [40].

6. NUMERICAL RESULTS

We now discuss a set of numerical experiments to demonstrate the performance of the proposed technique. We have two extraction (or production) wells: one well is situated along the diagonal, opposite to the injection well, and the other is situated at the center of a side that is one of the two sides that enclose the extraction (or production) well at the corner. In this configuration, we refer to them as corner and center wells, respectively (see Figs. 1 and 3).

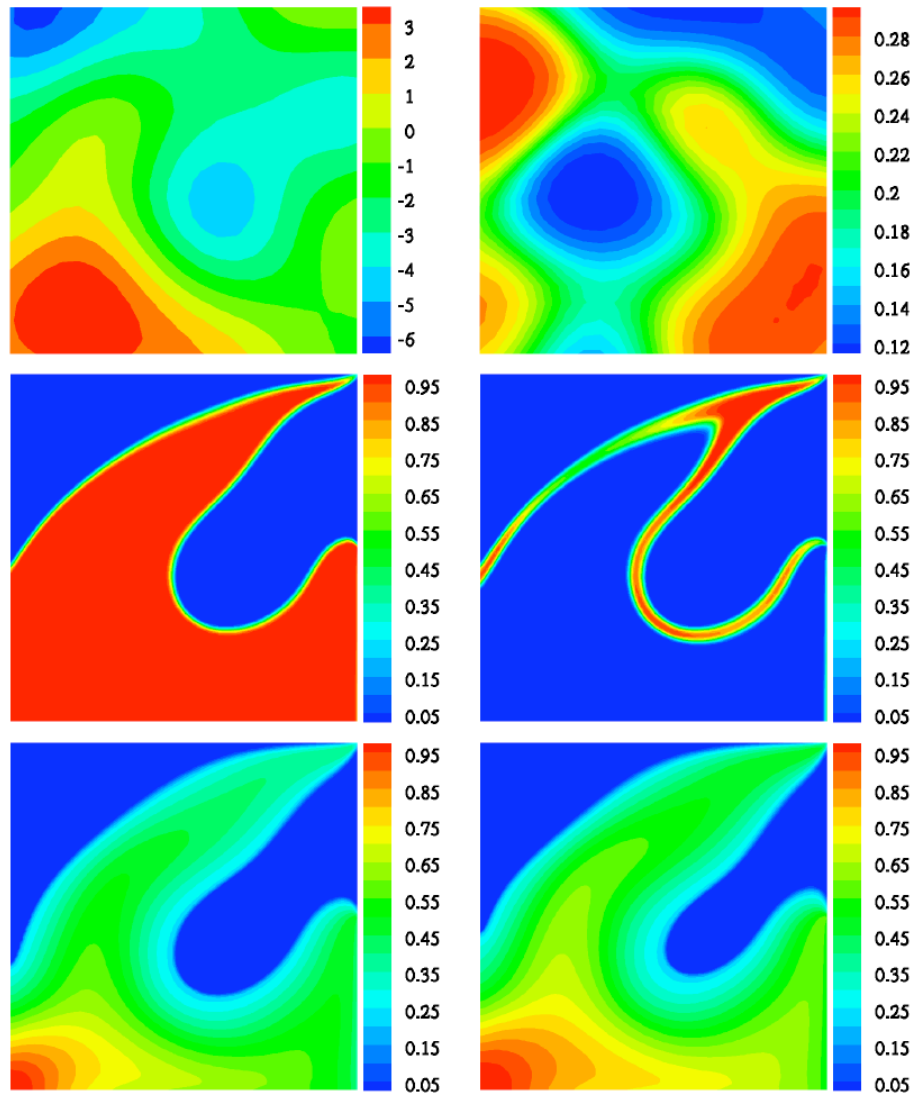


FIG. 3: Reference fields and corresponding flow patterns. Top: Permeability field (in logarithmic scale) on the left and porosity on the right. Middle: Single-phase flow pattern at $t = 0.7$ PVI (on the left injection of tracer until $t = 0.7$ PVI and on the right injection of tracer until $t = 0.15$ PVI). Bottom: Two-phase flow pattern (on the left at $t = 0.7$ PVI and on the right at $t = 1.4$ PVI).

6.1 Step I: Characterization

For the single-phase flow problem the tracer is injected at the injection well at the rate of one pore-volume every five years. To identify an efficient way of injecting the tracer from the characterization point of view (not considering the cost), we consider two cases: the continuous injection of tracer until $t = 0.7$ PVI and the injection of tracer until only $t = 0.15$ PVI (see Fig. 4). We assume that we have observed tracer data as curves at the extraction wells until 0.7 PVI. We use these curves to characterize the permeability and porosity fields in a two-stage MCMC method. In each case we also consider the effect of incorporating static data for the characterization, i.e., we use the values of permeability and porosity at the injection and production wells (see Section 4 to include static data in the Bayesian framework). We now have four cases: injection of tracer until $t = 0.7$ PVI with no static data, injection of tracer until $t = 0.15$ PVI with no static data, injection of tracer until $t = 0.7$ PVI with static data, and injection of tracer until $t = 0.15$ PVI with static data.

For KLE in (7), we select the correlation length $L_{xx} = L_{yy} = 0.2$, $L_{xy} = L_{yx} = 0$, and variance $\sigma_Y^2 = 4$. Figure 5 shows that the eigenvalues decay very fast for these values, and it is enough to consider the first twenty eigenpairs in the KLE. Since we assume that the permeability and porosity share the same spatial structure, we share the same KLE structure for the permeability and porosity fields, with $N_k = N_\phi = 20$. However, we model these fields as independent random fields, we propose θ^k and θ^ϕ separately in the Algorithm. Here, we generated reference fields of permeability and porosity on a fine grid of size 128×128 using a set of θ^k and θ^ϕ . The reference fields are

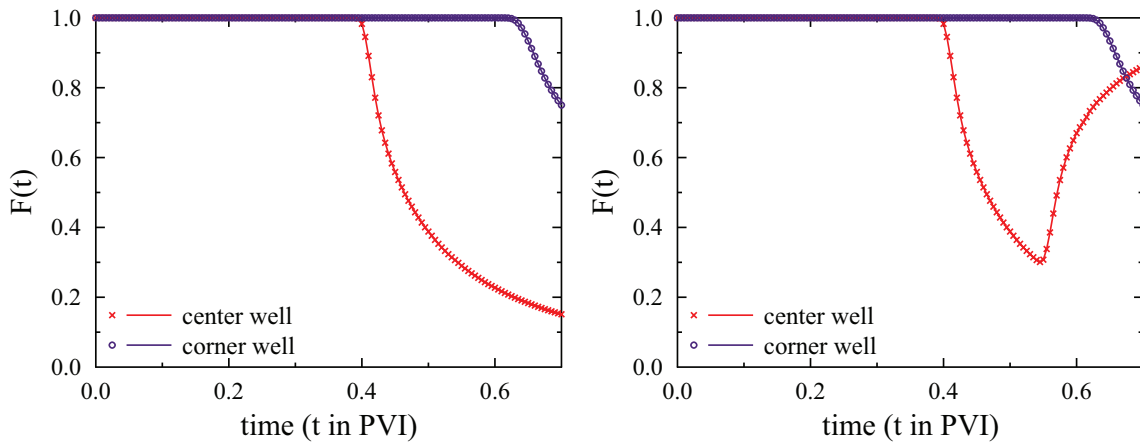


FIG. 4: Measured fractional flow curves. Left: Injection of tracer until $t = 0.7$ PVI. Right: Injection of tracer until $t = 0.15$ PVI.

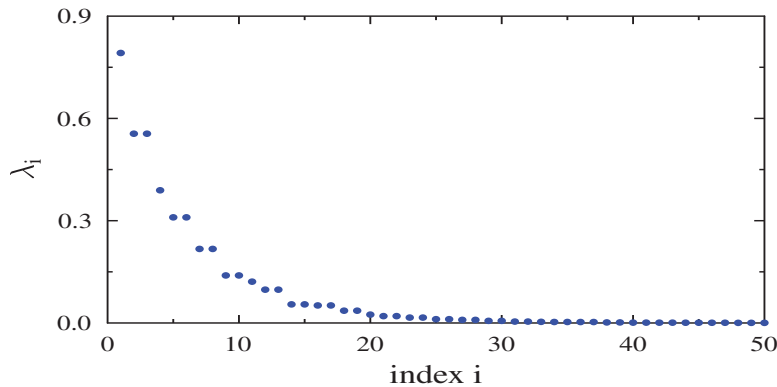


FIG. 5: Eigenvalues of the KLE for the Gaussian covariance with $L_{xx} = L_{yy} = 0.2$, $L_{xy} = L_{yx} = 0$, and $\sigma_Y^2 = 4$.

shown in Fig. 3. The simulator was then run forward to produce corresponding a reference fractional flow curve at each well (see Fig. 4).

Now, we turn our attention to σ_F^2 in the likelihood function (18). The σ_F^2 must be fixed a priori, because treating σ_F^2 as an unknown parameter results in an unacceptably large estimate [15]. The smaller the value of σ_F^2 , the better the sampled production curves are. If σ_F^2 is chosen to be too large, then the posterior will ignore the likelihood and simply draw from the prior; if σ_F^2 is too small, then the posterior probability exists only in extreme modes, which unrealistically restricts possible permeability and porosity configurations. It is ideal to specify σ_F^2 from the knowledge of the error in measuring permeabilities and porosities. However, it is common to take a user-specified value for σ_F^2 (see for example Oliver et al. [4]). Here, we specify $\sigma_F^2 = 10^{-4}$ and $\sigma_C^2 = 4 \times 10^{-4}$ for fine-scale and coarse-scale simulations, respectively, which were found to be working well for our simulations.

As indicated in [16, 17, 19], in the case of distinct model problems, the two-stage MCMC runs fewer fine-scale black-box simulations than the single-stage MCMC (see Table 1). Therefore, we use the two-stage MCMC for sampling of permeability and porosity fields with the tracer test data. In the two-stage MCMC, we choose a coarse grid of size 16×16 , which not only captures the general trend of the fractional curves (see Fig. 2), but also runs about eight times faster than the fine-grid simulation.

6.2 Step II: Prediction

The accepted realizations for permeability and porosity in Step I are used to run the forward problem for the two-phase (water and oil) model until 1.4 PVI. The relative permeability functions of water and oil take the form of s^2 and $(1 - s)^2$, respectively, and the viscosity ratio between water and oil is 1:20. We assume that at $t = 0$ the reservoir is saturated by oil without any water [i.e., $s(x, 0) = 0$]. The water is then injected at the injection well at the rate of one pore-volume every five years. We then aggregate the results of the forward problem. This average curve is referred to as the prediction of the production curve. The prediction curves are plotted using 1000, 2000, and 3000 accepted fine-scale realizations and given in Figs. 6–9.

As shown in Figs. 6 and 7, including the static data in the MCMC chain helps to improve the prediction of the breakthrough time, which is defined as the first time of arrival of water at a given production well. However, this may result in longer burn-in period in the MCMC chain. See the curve that corresponds to “injection until 0.7 PVI with static data” in Fig. 10. This is not the case for the curve that corresponds to “injection until 0.15 PVI with static data.”

Also, we notice that the injection pattern of tracer plays an important role in the characterization of subsurface. It is clear from Figs. 8 and 9 that the predictions of breakthrough time are more accurate if we inject the tracer for a shorter period. In particular, if we use the static data with the shorter injection as shown in Fig. 9, the predictions are not only more accurate for the breakthrough time, but also for the entire curve of the center and the corner wells. The better performance is attributed to the fact that a short time injection allows for incorporating more important flow properties, which may not be otherwise detected should longer time injection is used. Moreover, this is also an encouraging finding from efficiency standpoint, since short time injection is more cost affordable.

TABLE 1: A comparison of accepted proposals for single- and two-stage MCMCs

MCMC	Single-stage	Two-stage (16×16)
Proposals	2000	2000
σ_F^2	10^{-4}	10^{-4}
σ_C^2	—	4×10^{-4}
Coarse-scale acc.	—	556
Fine-scale acc.	177	107
Acc. rate	8.9%	19.2%

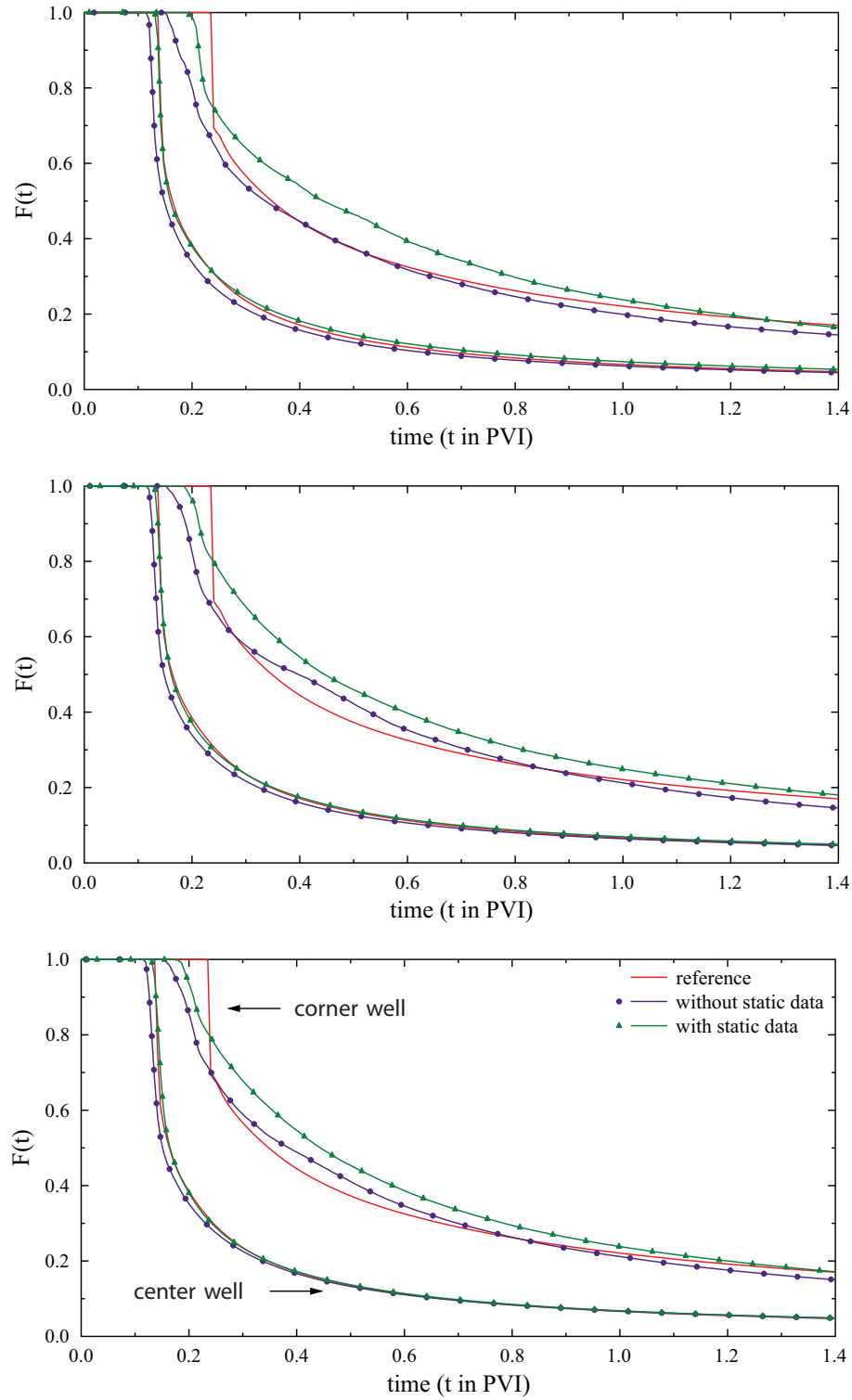


FIG. 6: Prediction curves — Tracer is injected until $t = 0.7$ PVI. From top to bottom, 1000, 2000, and 3000 accepted realizations used for prediction, respectively.

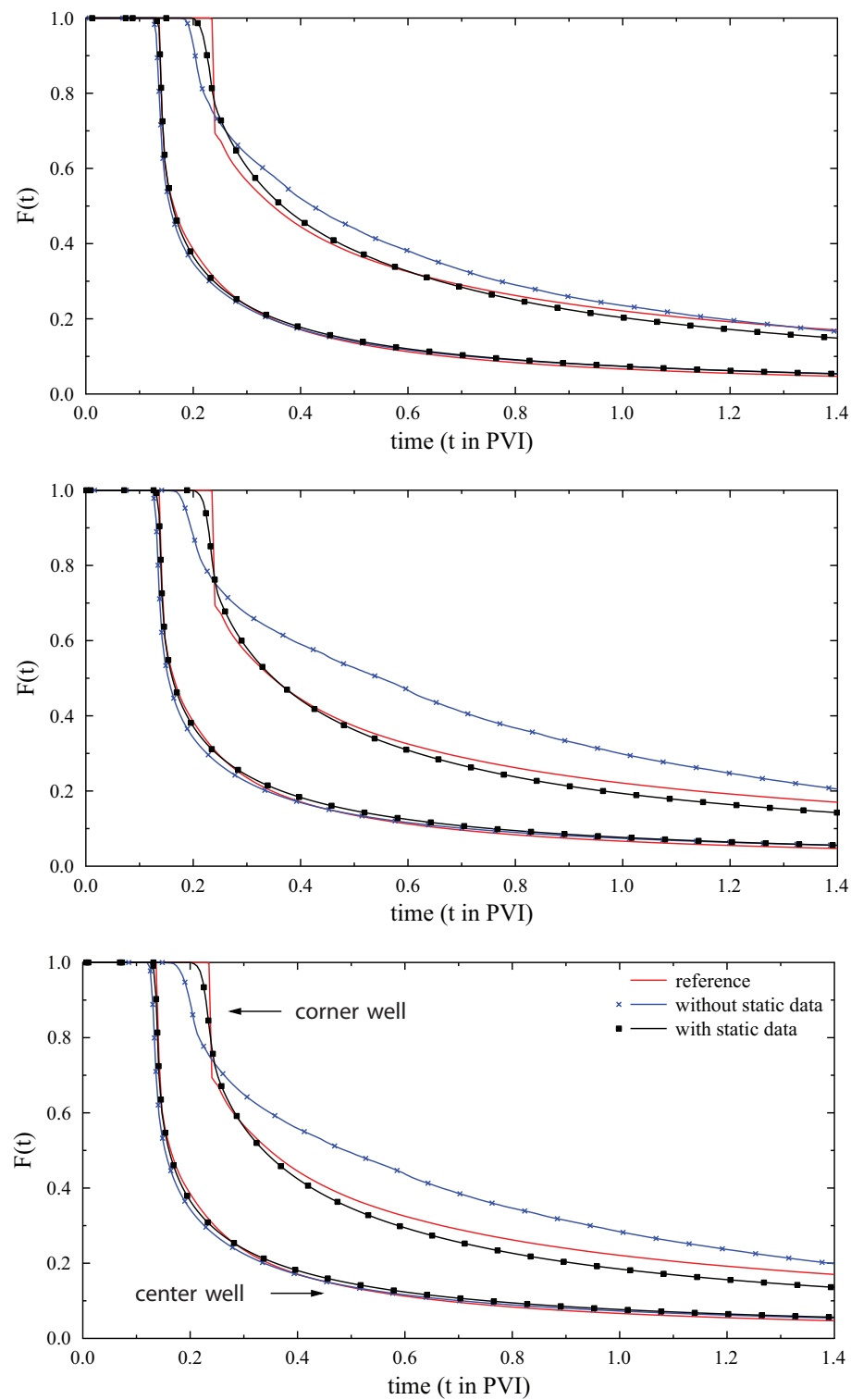


FIG. 7: Prediction curves — Tracer is injected until $t = 0.15$ PVI. From top to bottom, 1000, 2000, and 3000 accepted realizations used for prediction, respectively.

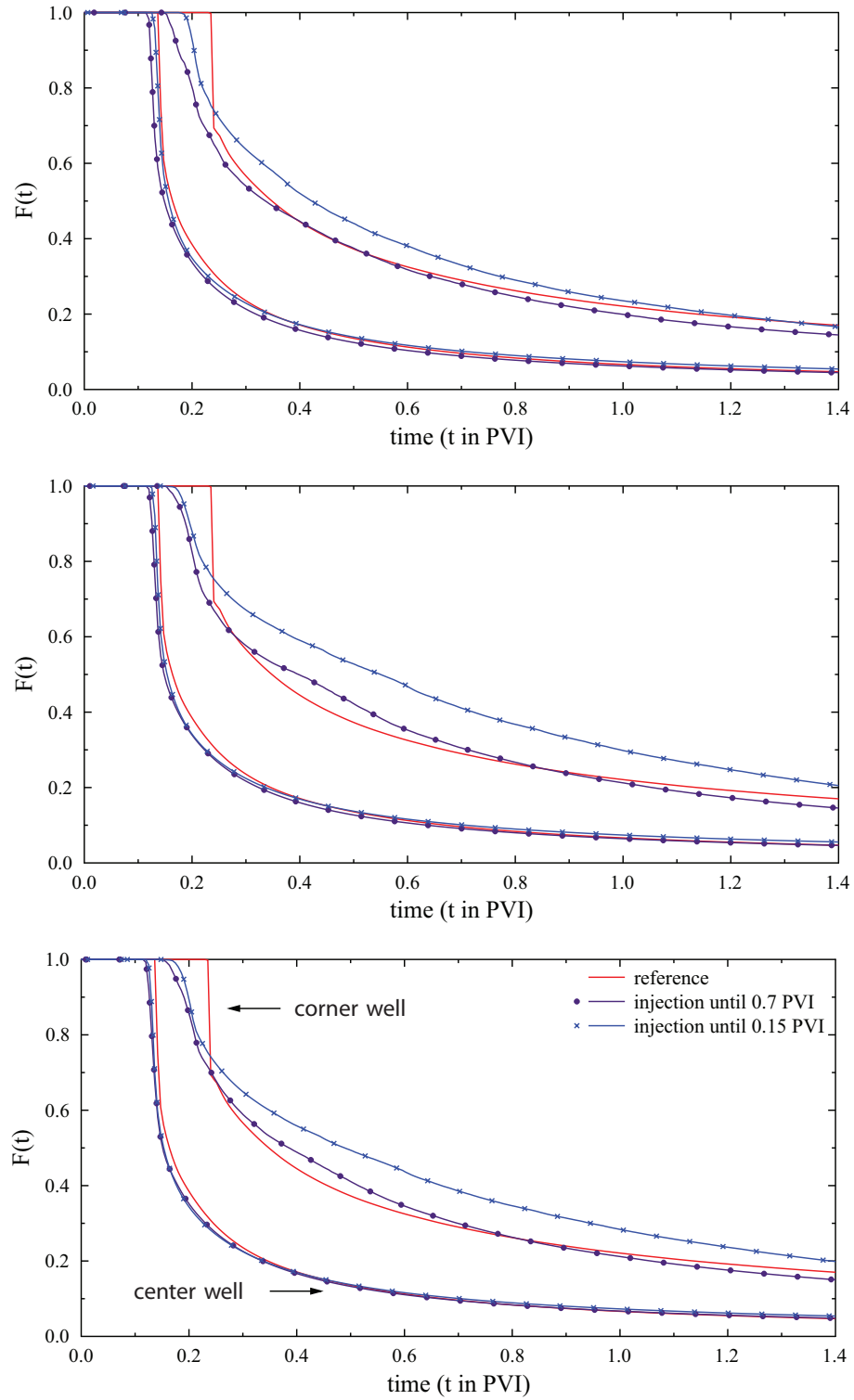


FIG. 8: Prediction curves — No permeability and porosity values at the wells are used. From top to bottom, 1000, 2000, and 3000 accepted realizations used for prediction, respectively.

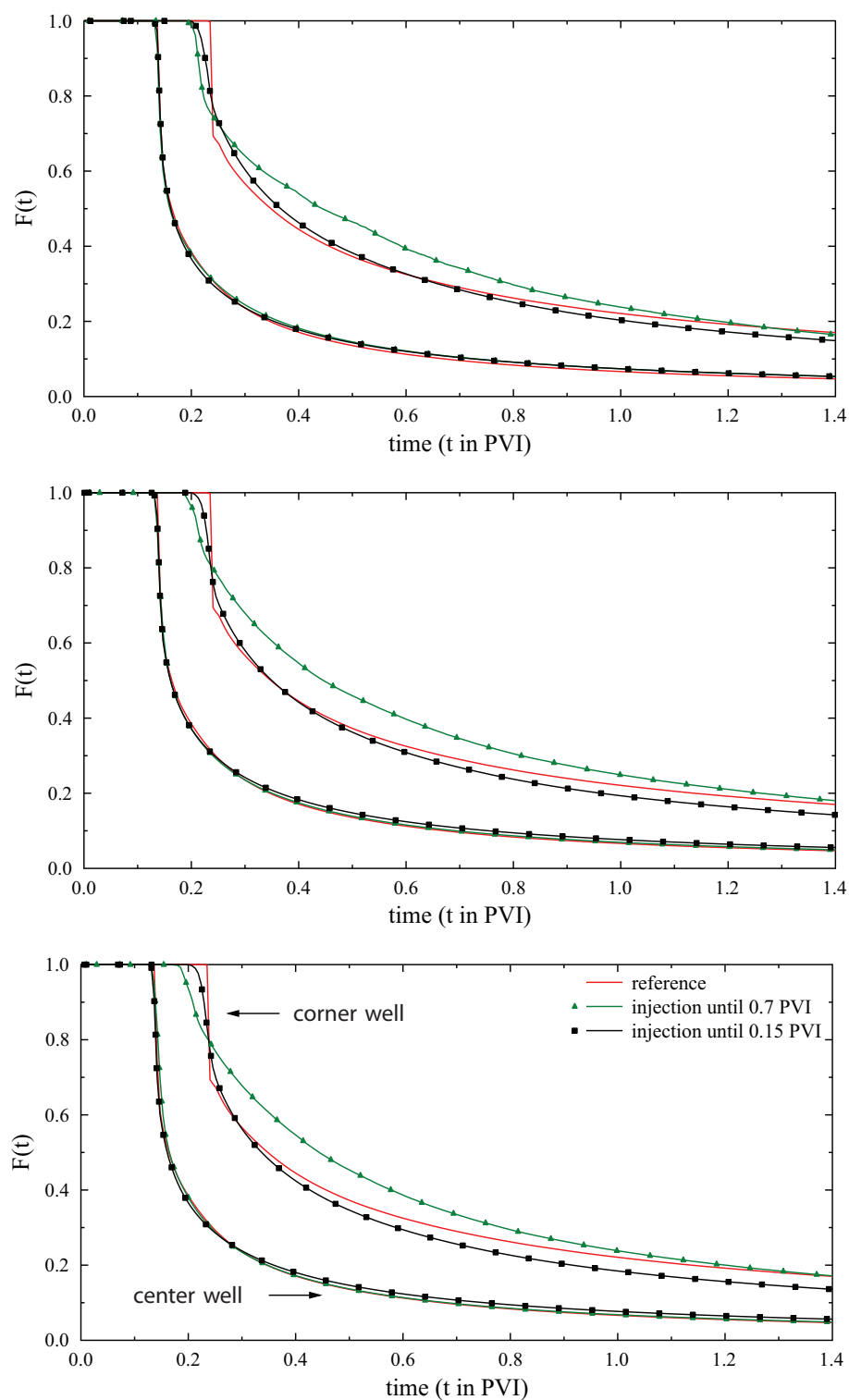


FIG. 9: Prediction curves — Permeability and porosity values at the wells are used. From top to bottom, 1000, 2000, and 3000 accepted realizations used for prediction, respectively.

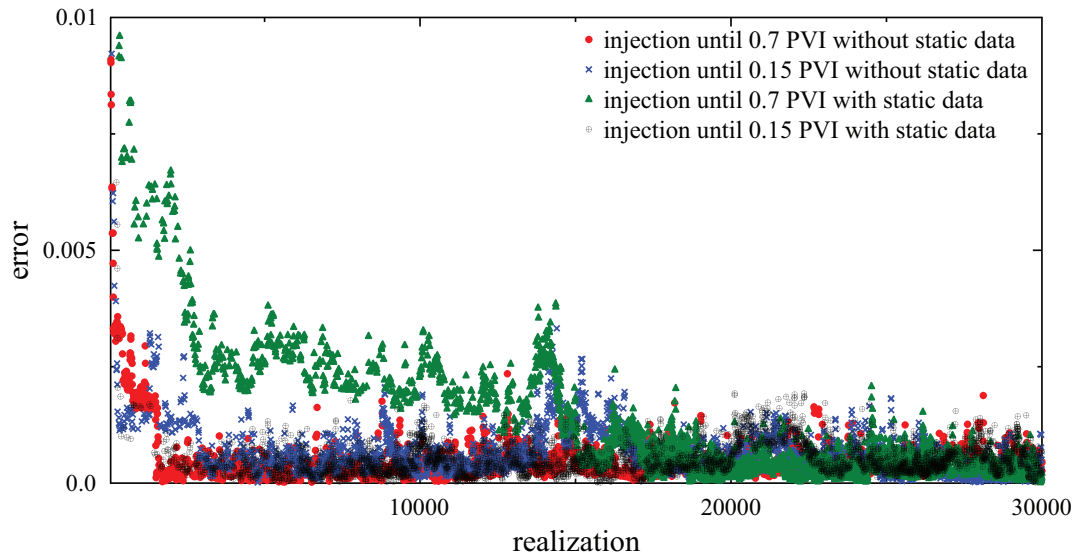


FIG. 10: A comparison of fractional flow error with accepted realization.

In Fig. 11 we give the upper and lower bounds of the standard deviation at a particular data point in the prediction curve for the case “injection of tracer until $t = 0.15$ PVI with static data.” For the center well the reference curve almost entirely lies between the upper and lower bounds, and for the corner well most part of the reference curve falls between the bounds.

The breakthrough time gives a good summary of the entire production curve [41]. In Fig. 12, kernel density functions for breakthrough times of accepted production curves are shown. For the center well, in all the cases, we predict the breakthrough time very accurately. For the corner well, the prediction based on the characterization in which the tracer is injected until 0.15 PVI and static data is included in the posterior exploration is more accurate, and it predicts that the simulated breakthrough time with the highest probability occurs precisely at the reference/measured breakthrough.

7. CONCLUSIONS

We described a predictive simulation technique in subsurface flow that utilizes single- and two-phase models and Bayesian MCMC, and discussed numerical results demonstrating its performance. In this technique, the tracer test (single-phase flow) was used for characterizing the subsurface, and based on the characterization we predicted the entire production curves of the two-phase flow.

It is well known that the injection of a tracer continuously is not economically feasible and injection of the tracer for a shorter time period is very practical. Numerical results also suggest that the later approach associated with the use of permeability and porosity values at some locations in the reservoir helps for a better characterization than the former.

The breakthrough time often hints the behavior of the entire production curve, and the technique presented in this paper accurately predicted the breakthrough times for both center and corner wells. This technique, which relies on a “tracer test,” is very adaptable for the practices in geothermal and petroleum industries. Tracer testing is simply a means for characterizing the subsurface. The numerical experiments show that the prediction based on the characterization can be very reliable and potentially offers an efficient procedure in more complex subsurface flow scenarios.

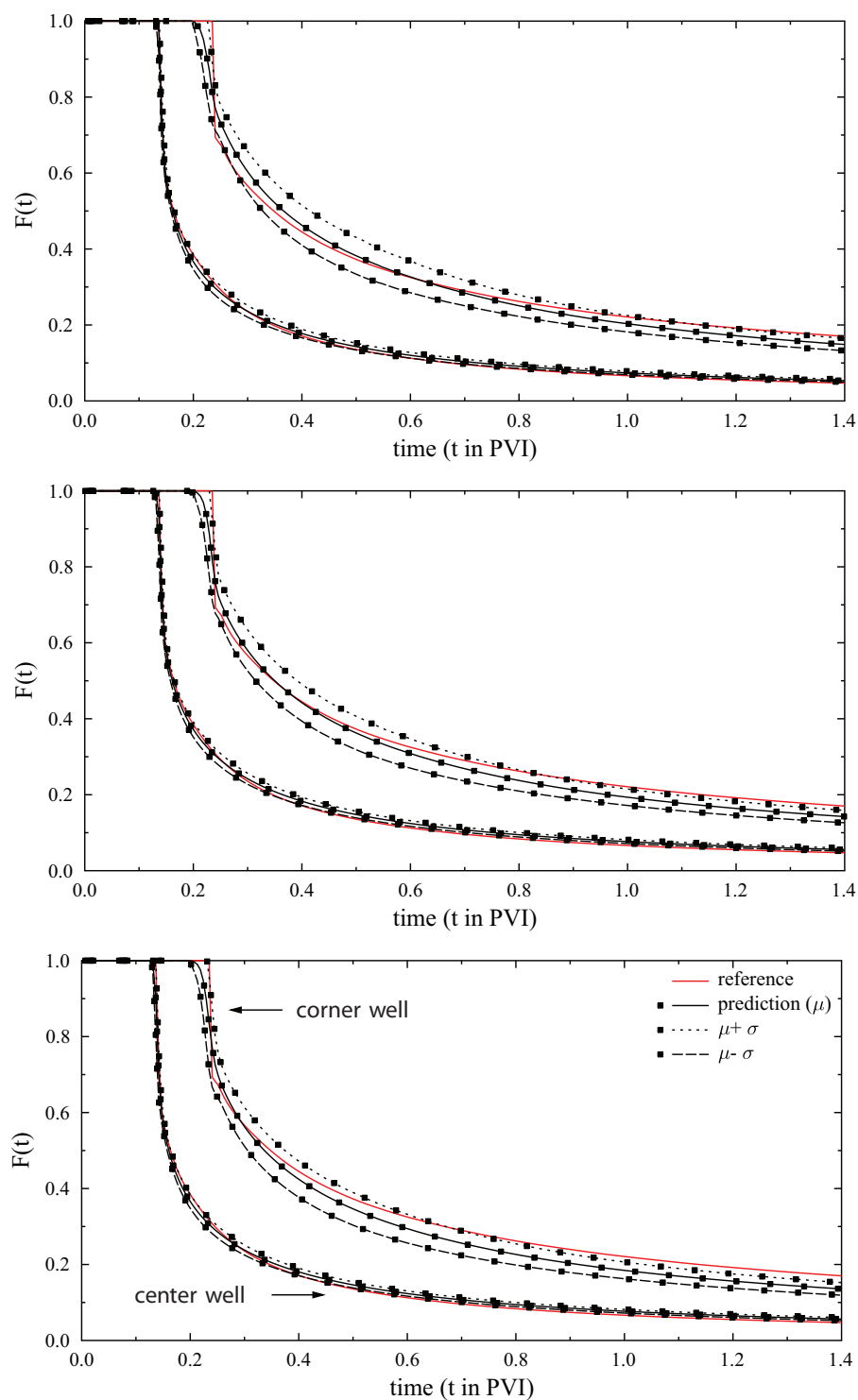


FIG. 11: Prediction curves for the case in which for the characterization, permeability, and porosity values at the wells are used, and the tracer is injected until $t = 0.15$ PVI. Mean production curves are referred as prediction curves. Upper and lower bounds of the standard deviation at a particular data point in the prediction curve are also given.

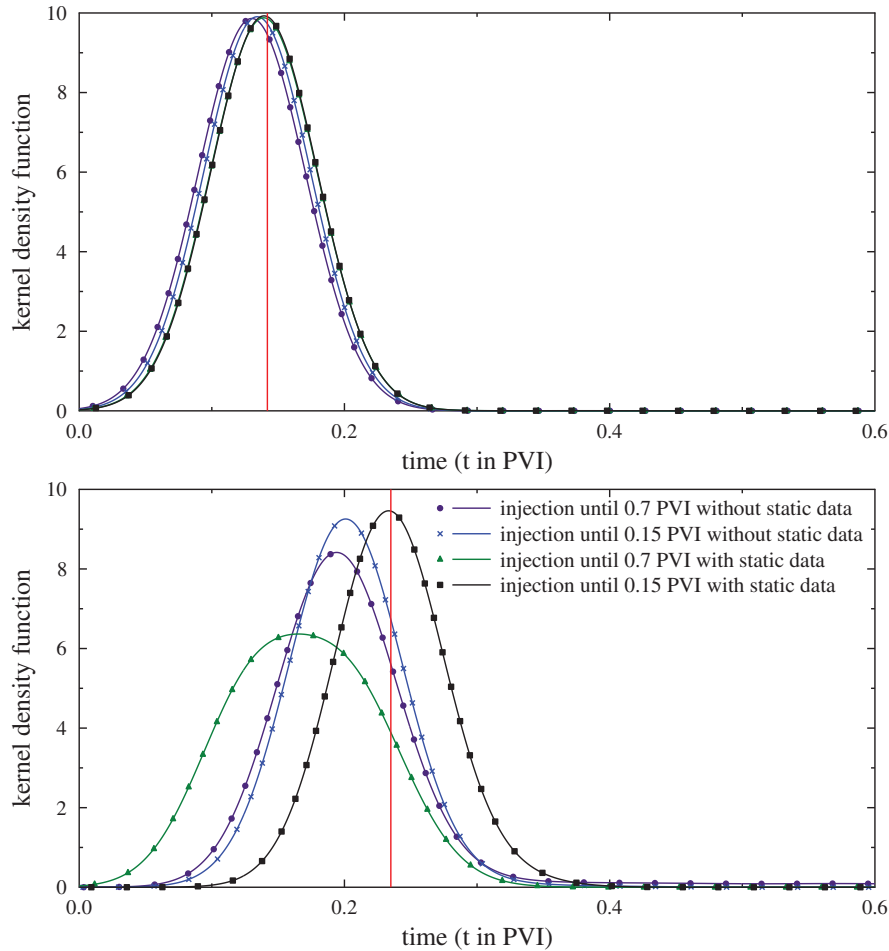


FIG. 12: Breakthrough times — Top: Center well. Bottom: Corner well.

ACKNOWLEDGMENTS

This work is partially supported by the grants from DOE (DE-FE0004832 and DE-SC0004982), the Center for Fundamentals of Subsurface Flow of the School of Energy Resources of the University of Wyoming (WYDEQ49811GNTG, WYDEQ49811PER, WYDEQ49811FRTD), 2011 Clean Coal Technologies Research Program of the School of Energy Resources of the University of Wyoming (1100 20352 2012), and from NSF (DMS-1016283). This work was done while the third author was in the Department of Mathematics at the University of Wyoming.

REFERENCES

1. Ma, S. and Morrow, N., Relationships between Porosity and Permeability for Porous Rocks, *International Symposium of the Society of Core Analysts*, Montpellier, France, Sept. 8–10, 1996.
2. Sperl, J. and Trckova, J., Permeability and porosity of rocks and their relationship based on laboratory testing, *Acta Geodyn. Geomater.*, 5(1):41–47, 2008.
3. Jin, M., Delshad, M., Dwarakanath, V., McKinney, D., Pope, G., Sepehrnoori, K., Tilburg, C., and Jackson, R., Partitioning tracer test for detection, estimation, and remediation performance assessment of subsurface non-aqueous phase liquids, *Water Resour. Res.*, 31:1201–1211, 1995.

4. Oliver, D., Cunha, L., and Reynolds, A., Markov chain Monte Carlo methods for conditioning a permeability field to pressure data, *Math. Geol.*, 29(1):61–91, 1997.
5. Datta-Gupta, A., Yoon, S., Barman, I., and Vasco, D., Streamline-based production-data integration into high-resolution reservoir models, *J. Petr. Tech.*, 50(12):72–75, 1999.
6. Datta-Gupta, A., Streamline simulation: A technology update, *J. Petr. Tech.*, 52(12):68–73, 2000.
7. Wang, Y. and Kovscek, A., Streamline approach for history matching production data, *Soc. Petr. Eng. J.*, 5(4):353–362, 2000.
8. Abbaszadeh-Dehghani, M. and Brigham, W., Analysis of well-to-well tracer flow to determine reservoir layering, *J. Petr. Tech.*, 36(10):1753–1762, 1984.
9. Lake, L., *Enhanced Oil Recovery*, Prentice Hall, Englewood Cliffs, NJ, 1989.
10. Kass, W., *Tracing Technique in Geohydrology*, A. A. Balkema Publishers, Brookfield, VT, 1998.
11. Agca, C., Pope, G., and Sepehrnoori, K., Modelling and analysis of tracer flow in oil reservoirs, *J. Petr. Sci. Eng.*, 4:3–19, 1990.
12. Zemel, B., *Tracers in the Oil Field*, Elsevier Science, Amsterdam, Netherlands, 1995.
13. Shook, G., Ansley, S., and Wyile, A., Tracers and tracer testing: Design, implementation, and interpretation methods, Tech. Rep. INEEL/EXT-03-01466, Idaho National Engineering and Environmental Laboratory, Idaho Falls, ID 83415, USA, January 2004.
14. Rieckermann, J., Borsuk, M., Sydler, D., Gujer, W., and Reichert, P., Bayesian experimental design of tracer studies to monitor wastewater leakage from sewer networks, *Water Resour. Res.*, 46(8):W08513, 2010.
15. Lee, H., Higdon, D., Bi, Z., Ferreira, M., and West, M., Markov random field models for high-dimensional parameters in simulations of fluid flow in porous media, *Technomet.*, 44(3):230–241, 2002.
16. Ma, X., Al-Harbi, M., Datta-Gupta, A., and Efendiev, Y., An efficient two-stage sampling method for uncertainty quantification in history matching geological models, *SPE J.*, 13(1):77–87, 2008.
17. Efendiev, Y., Datta-Gupta, A., Ginting, V., Ma, X., and Mallick, B., An efficient two-stage Markov chain Monte Carlo method for dynamic data integration, *Water Resour. Res.*, 41(12):W12423, 2005.
18. Douglas, C., Efendiev, Y., Ewing, R., Ginting, V., and Lazarov, R., Dynamic data driven simulations in stochastic environments, *Comput.*, 77(4):321–333, 2006.
19. Efendiev, Y., Hou, T., and Luo, W., Preconditioning Markov chain Monte Carlo simulations using coarse-scale models, *SIAM J. Sci. Comput.*, 28(2):776–803, 2006.
20. Loève, M., *Probability theory*, Springer, Berlin, 1977.
21. Higdon, D., Lee, H., and Bi, Z., A Bayesian approach to characterizing uncertainty in inverse problems using coarse and fine-scale information, *IEEE Trans. Signal Proc.*, 50:389–399, 2002.
22. Fox, C. and Nicholls, G. Sampling conductivity images via MCMC, Mardia, K., Gill, C., and Aykroyd, R. (Eds.), *The art and science of Bayesian image analysis, Proceedings of the Leeds Annual Statistics Research Workshop*, pp. 91–100. University of Leeds, 1997.
23. Christen, J. A. and Fox, C., Markov chain Monte Carlo using an approximation, *J. Comput. Graphical Stat.*, 14(4):795–810, 2005.
24. Ginting, V., Pereira, F., and Rahunathan, A., Multi-stage Markov chain Monte Carlo methods for porous media flows, *1st International Symposium on Uncertainty Quantification and Stochastic Modeling (Uncertainties 2012)*, Maresias, Sao Sebastiao, SP, Brazil, February 26–March 2, 2012.
25. Pereira, F. and Rahunathan, A., Numerical simulation of two-phase flows on a GPU, *9th International meeting on High Performance Computing for Computational Science (VECPAR'10)*, Berkeley, CA, June 2010.
26. Chen, Z., Huan, G., and Ma, Y., *Computational Methods for Multiphase Flows in Porous Media*, SIAM, Philadelphia, PA, 2006.
27. Douglas Jr., J., Furtado, F., and Pereira, F., On the numerical simulation of waterflooding of heterogeneous petroleum reservoirs, *Comput. Geosci.*, 1:155–190, 1997.
28. Abreu, E., Douglas Jr., J., Furtado, F., and Pereira, F., Operator splitting based on physics for flow in porous media, *Int. J. Comput. Sci.*, 2(3):315–335, 2008.

29. Abreu, E., Douglas Jr., J., Furtado, F., and Pereira, F., Operator splitting for three-phase flow in heterogeneous porous media, *Commun. Comput. Phys.*, 6(1):72–84, 2009.
30. Aquino, A., Pereira, T., Francisco, A., Pereira, F., and Amaral Souto, H., A Lagrangian strategy for the numerical simulation of radionuclide transport problems, *Prog. Nuclear Energy*, 52 (3):282–291, 2010.
31. Raviart, P. and Thomas, J., A mixed finite element method for 2nd order elliptic problems, Galligani, I. and Magenes, E. (Eds.), *Mathematical Aspects of Finite Element Methods*, Vol. 606 of Lecture Notes in Mathematics, pp. 292–315, Springer Berlin, Heidelberg, 1977.
32. Liebmann, M., Efficient PDE solvers on modern hardware with applications in medical and technical sciences, PhD thesis, University of Graz, 2009.
33. Kurganov, A. and Tadmor, E., New high-resolution central schemes for nonlinear conservation laws and convection-diffusion equations, *J. Comput. Phys.*, 160:241–282, 2000.
34. Pereira, F. and Rahunanthan, A., A semi-discrete central scheme for the approximation of two-phase flows in three space dimensions, *Math. Comput. Simul.*, 81(10):2296–2306, 2011.
35. Wong, E., *Stochastic Processes in Information and Dynamical Systems*, McGraw-Hill, New York, 1971.
36. Ginting, V., Pereira, F., Prescho, M., and Wo, S., Application of the two-stage Markov chain Monte Carlo method for characterization of fractured reservoirs using a surrogate flow model, *Comput. Geosci.*, 15(4):691–707, 2011.
37. Dagan, G., *Flow and Transport in Porous Formations*, Springer-Verlag, 1989.
38. Frauenfelder, P., Schwab, C., and Todor, R., Finite elements for elliptic problems with stochastic coefficients, *Comput. Methods Appl. Mech. Eng.*, 194:205–228, 2005.
39. Durlofsky, L., Numerical calculation of equivalent grid block permeability tensors for heterogeneous porous media, *Water Resour. Res.*, 27(5):699–708, 1991.
40. Gamerman, D. and Lopes, H., Markov Chain Monte Carlo—Stochastic simulation for Bayesian inference, Vol. 68 of Texts in Statistical Science, Chapman & Hall/CRC, 2nd edition, 2006.
41. Vasco, D. and Datta-Gupta, A., Asymptotic solutions for solute transport: A formalism for tracer tomography, *Water Resour. Res.*, 35(1):1–16, 1999.
42. Nessyahu, N. and Tadmor, E., Non-oscillatory central differencing for hyperbolic conservation laws, *J. Comput. Phys.*, 87(2):408–463, 1990.
43. Kurganov, A. and Petrova, G., A third-order semi-discrete genuinely multidimensional central scheme for hyperbolic conservation laws and related problems, *Numer. Math.*, 88(4):683–729, 2001.
44. Shu, C.-W. and Osher, S., Efficient implementation of essentially nonoscillatory shock-capturing schemes II, *J. Comput. Phys.*, 83(1):32–78, 1989.

APPENDIX A. A SEMI-DISCRETE SCHEME FOR DISCONTINUOUS COEFFICIENTS

In this section we outline the derivation of a second-order, semi-discrete, central scheme for the one-dimensional, scalar conservation laws of the form

$$\phi(x) \frac{\partial u}{\partial t} + \frac{\partial f(u)}{\partial x} = 0, \quad (\text{A.1})$$

subject to the initial condition

$$u(x, t = 0) = u_0(x), \quad (\text{A.2})$$

where $u \in \mathbb{R}$, $f(u)$ is a nonlinear flux, and $\phi(x)$ is a piecewise constant function of x with $\phi(x) > 0$. Since we consider solving problems arising in two-phase flow, we derive the scheme for the scalar conservation law. The derivation has a simple extension to systems of conservation law. Moreover, the derivation is based on the Nessyahu–Tadmor (NT) and Kurganov–Tadmor (KT) central schemes proposed in [33, 42, 43], and here we give the outline of the procedure.

Define $x_i := i\Delta x$, $x_{i\pm\frac{1}{2}} := x_i \pm \Delta x/2$. Assume that we have already computed an approximation to the solution at time level $t = t^n$ —a piecewise linear approximation $\tilde{u}(x, t^n) \approx u(x, t^n)$ of the form

$$\tilde{u}(x, t^n) := \sum_i p_i^n(x) \chi_i(x), \quad (\text{A.3})$$

where

$$p_i^n(x) = \bar{u}_i^n + (u_x)_i^n (x - x_i), \quad (\text{A.4})$$

with slopes are approximated by MinMod limiter, χ_i is the characteristic function of the corresponding region, and \bar{u}_i is the cell average defined by

$$\bar{u}_i := \frac{1}{\Delta x} \int_{x_{i-1/2}}^{x_{i+1/2}} \tilde{u}(\xi, t^n) d\xi. \quad (\text{A.5})$$

We now derive the semi-discrete scheme for discontinuous coefficients ϕ_i considering a dual grid approach, in which $\phi(x)$ is defined on the given grid and the solution is computed on a modified grid (this is one of the original contributions of the new scheme presented here that allows us to handle solution discontinuities away from porosity discontinuities).

We define

$$\phi_{i+1/2} := \phi(x), \quad x \in [x_i, x_{i+1}], \quad \forall i, \quad (\text{A.6})$$

and ϕ_i is a piecewise constant. We begin with the piecewise linear reconstruction $\{p_i^n\}$, which may have discontinuities at $\{x_{i+1/2}\}$. We compute the maximum local speed of propagation of the discontinuities by

$$a_{i+1/2}^n := \frac{1}{\phi_{i+1/2}} \left(\max_{\omega \in \mathcal{C}(u_{i-1/2}^+, u_{i+1/2}^-)} \frac{\partial f}{\partial u}(\omega) \right), \quad (\text{A.7})$$

where $\mathcal{C}(u_{i+1/2}^+, u_{i-1/2}^-)$ is the curve that connects $u_{i+1/2}^+$ and $u_{i-1/2}^-$, and $u_{i+1/2}^+ := p_{i+1}^n(x_{i+1/2})$ and $u_{i-1/2}^- := p_i^n(x_{i+1/2})$. We consider the domains in Figure A.13

$$\begin{aligned} & [x_{i-1/2,r}^n, x_i - \epsilon \Delta t^2] \times [t^n, t^{n+1}], \quad [x_i - \epsilon \Delta t^2, x_i + \epsilon \Delta t^2] \times [t^n, t^{n+1}], \\ & [x_i + \epsilon \Delta t^2, x_{i+1/2,l}^n] \times [t^n, t^{n+1}] \quad \text{and} \quad [x_{i+1/2,l}^n, x_{i+1/2,r}^n] \times [t^n, t^{n+1}] \end{aligned} \quad (\text{A.8})$$

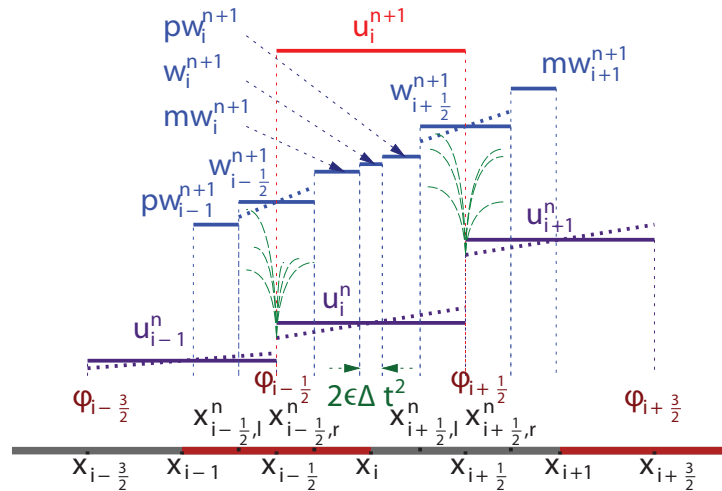


FIG. A.13: Central differencing with discontinuous porosity coefficients.

with

$$x_{i+1/2,l}^n := x_{i+1/2} - \Delta t a_{i+1/2}^n \text{ and } x_{i+1/2,r}^n := x_{i+1/2} + \Delta t a_{i+1/2}^n. \quad (\text{A.9})$$

Since in the interval $[x_{i+1/2,l}^n, x_{i+1/2,r}^n]$ the value of ϕ is constant, we can compute the cell average $\bar{w}_{i+1/2}^{n+1}$ as

$$\begin{aligned} \bar{w}_{i+1/2}^{n+1} &:= \frac{1}{\Delta x_{i+1/2}} \int_{x_{i+1/2,l}^n}^{x_{i+1/2,r}^n} u(\xi, t^{n+1}) d\xi = \frac{\bar{u}_i^n + \bar{u}_{i+1}^n}{2} + \frac{\Delta x - a_{i+1/2}^n \Delta t}{4} \{(u_x)_i^n - (u_x)_{i+1}^n\} \\ &\quad - \frac{1}{2a_{i+1/2}^n \phi_{i+1/2}} \left[f(u_{i+1/2,r}^{n+1/2}) - f(u_{i+1/2,l}^{n+1/2}) \right]. \end{aligned} \quad (\text{A.10})$$

Let us now focus on the cell average in the interval $[x_{i-1/2}^n, x_{i+1/2}^n]$. We want to use an appropriate quadrature rule to approximate the flux integrals at $x = x_i$. The discontinuity in ϕ at $x = x_i$ causes the solution u to lose differentiability at x_i and the solution is not smooth along the line $x = x_i$. Therefore, we introduce the cell $[x_i - \epsilon \Delta t^2, x_i + \epsilon \Delta t^2]$ of width $2\epsilon \Delta t^2$ at x_i . Now, we can use the quadrature rule along the vertical lines $x = x_i - \epsilon \Delta t^2$ and $x = x_i + \epsilon \Delta t^2$. Let us exactly compute the following integral, which is related to \bar{w}_i^{n+1} as

$$\begin{aligned} &\frac{1}{2\epsilon \Delta t^2} \int_{x_i - \epsilon \Delta t^2}^{x_i + \epsilon \Delta t^2} \phi(\xi) u(\xi, t^{n+1}) d\xi \\ &= \frac{1}{2\epsilon \Delta t^2} \left[\phi_{i-1/2} \int_{x_i - \epsilon \Delta t^2}^{x_i} u(\xi, t^n) d\xi + \phi_{i+1/2} \int_{x_i}^{x_i + \epsilon \Delta t^2} u(\xi, t^n) d\xi \right] \\ &\quad - \frac{1}{2\epsilon \Delta t^2} \int_{t^n}^{t^{n+1}} [f(u(x_i + \epsilon \Delta t^2, \tau)) - f(u(x_i - \epsilon \Delta t^2, \tau))] d\tau. \end{aligned} \quad (\text{A.11})$$

With the simple arithmetic manipulation, we can write the integral in the left-hand side of (A.11) as

$$\begin{aligned} &\int_{x_i - \epsilon \Delta t^2}^{x_i + \epsilon \Delta t^2} \phi(\xi) u(\xi, t^{n+1}) d\xi = \frac{\phi_{i-1/2} + \phi_{i+1/2}}{2} \int_{x_i - \epsilon \Delta t^2}^{x_i + \epsilon \Delta t^2} u(\xi, t^{n+1}) d\xi \\ &\quad + \frac{\phi_{i-1/2} - \phi_{i+1/2}}{2} \left[\int_{x_i - \epsilon \Delta t^2}^{x_i} u(\xi, t^{n+1}) d\xi - \int_{x_i}^{x_i + \epsilon \Delta t^2} u(\xi, t^{n+1}) d\xi \right]. \end{aligned} \quad (\text{A.12})$$

Though, at $x = x_i$ the solution $u(\xi, t^{n+1})$ loses differentiability, the continuity of the solution is maintained. Therefore, as $\Delta t \rightarrow 0$

$$\mathcal{R}_i := \frac{\phi_{i-1/2} - \phi_{i+1/2}}{\phi_{i-1/2} + \phi_{i+1/2}} \left[\int_{x_i - \epsilon \Delta t^2}^{x_i} u(\xi, t^{n+1}) d\xi - \int_{x_i}^{x_i + \epsilon \Delta t^2} u(\xi, t^{n+1}) d\xi \right] \rightarrow 0. \quad (\text{A.13})$$

Therefore, we can write \bar{w}_i^{n+1} as

$$\begin{aligned} \bar{w}_i^{n+1} &:= \frac{1}{2\epsilon \Delta t^2} \int_{x_i - \epsilon \Delta t^2}^{x_i + \epsilon \Delta t^2} u(\xi, t^{n+1}) d\xi = \frac{(\phi_{i-1/2} + \phi_{i+1/2})}{(\phi_{i-1/2} + \phi_{i+1/2})} \bar{u}_i \\ &\quad - \frac{(\phi_{i-1/2} - \phi_{i+1/2})\epsilon \Delta t^2}{2(\phi_{i-1/2} + \phi_{i+1/2})} (u_x)_i - \frac{1}{(\phi_{i-1/2} + \phi_{i+1/2})\epsilon \Delta t} \\ &\quad \times \left[f(u^{n+1/2}(x_i + \epsilon \Delta t^2)) - f(u^{n+1/2}(x_i - \epsilon \Delta t^2)) \right] + \frac{1}{2\epsilon \Delta t^2} \mathcal{R}_i. \end{aligned} \quad (\text{A.14})$$

We can write $p\bar{w}_i^{n+1}$ as

$$\begin{aligned} p\bar{w}_i^{n+1} := & \frac{1}{(\Delta x/2 - a_{i+1/2}^n \Delta t - \epsilon \Delta t^2)} \int_{x_i + \epsilon \Delta t^2}^{x_{i+1/2}^n} u(\xi, t^{n+1}) d\xi = \bar{u}_i - \frac{\Delta x/2 - a_{i+1/2}^n \Delta t + \epsilon \Delta t^2}{2} (u_x)_i \\ & - \frac{\Delta t}{\phi_{i+1/2}(\Delta x/2 - a_{i+1/2}^n \Delta t - \epsilon \Delta t^2)} \left[f(u_{i+1/2}^{n+1}) - f(u^{n+1/2}(x_i + \epsilon \Delta t^2)) \right]. \end{aligned} \quad (\text{A.15})$$

To obtain the cell averages over the original grid of the uniform, non-staggered cells $[x_{i-1/2}, x_{i+1/2}]$, we consider the piecewise linear reconstruction over non-uniform cells of the form

$$\begin{aligned} \tilde{w}(x, t^{n+1}) := & \sum_j \{ [\bar{w}_{i+1/2}^{n+1} - (u_x)_{i+1/2}^{n+1} (x - x_{i+1/2})] \mathbf{1}_{[x_{i+1/2}^n, x_{i+1/2}^n]} \\ & + p\bar{w}_i^{n+1} \mathbf{1}_{[x_i + \epsilon \Delta t^2, x_{i+1/2}^n]} + \bar{w}_i^{n+1} \mathbf{1}_{[x_i - \epsilon \Delta t^2, x_i + \epsilon \Delta t^2]} \\ & + m\bar{w}_i^{n+1} \mathbf{1}_{[x_{i-1/2}^n, x_i - \epsilon \Delta t^2]} \}, \end{aligned} \quad (\text{A.16})$$

with $u_x(x_{i+1/2}, t^{n+1})$ are approximated by

$$(u_x)_{i+1/2}^{n+1} = \text{minmod} \left(\frac{w_{i+1}^{n+1} - w_{i+1/2}^{n+1}}{\Delta X}, \frac{w_{i+1/2}^{n+1} - p\bar{w}_i^{n+1}}{\Delta X} \right), \quad (\text{A.17})$$

where

$$\Delta X = \frac{\Delta x/2 + \Delta t a_{i+1/2}^n - \epsilon \Delta t^2}{2}. \quad (\text{A.18})$$

Here, we do not need to reconstruct the average of the smooth portions $m\bar{w}_i^{n+1}$ and $p\bar{w}_i^{n+1}$ of the solution. Also, we can skip reconstructing the portion w_i^{n+1} of the solution, where the solution is continuous, but is not differentiable. Now we can write the fully discrete second-order central scheme as

$$\begin{aligned} \bar{u}_i^{n+1} = & \frac{1}{\Delta x} \int_{x_{i-1/2}}^{x_{i+1/2}} \tilde{w}(\xi, t^{n+1}) d\xi = \frac{a_{i-1/2}^n \Delta t}{\Delta x} \bar{w}_{i-1/2}^{n+1} + \frac{(\Delta x/2 - a_{i-1/2}^n \Delta t - \epsilon \Delta t^2)}{\Delta x} m\bar{w}_i^{n+1} \\ & + \frac{2\epsilon \Delta t^2}{\Delta x} \bar{w}_i^{n+1} + \frac{(\Delta x/2 - a_{i+1/2}^n \Delta t - \epsilon \Delta t^2)}{\Delta x} p\bar{w}_i^{n+1} + \frac{a_{i+1/2}^n \Delta t}{\Delta x} \bar{w}_{i+1/2}^{n+1} + \mathcal{O}(\Delta t^2) \end{aligned} \quad (\text{A.19})$$

We substitute \bar{u}_i^{n+1} from the fully discrete scheme (A.19) in

$$\frac{d\bar{u}_i}{dt} = \lim_{\Delta t \rightarrow 0} \frac{\bar{u}_i^{n+1} - \bar{u}_i^n}{\Delta t}, \quad (\text{A.20})$$

and take $\Delta t \rightarrow 0$ with fixed Δx . By rearranging the terms we can write the semi-discrete central scheme as

$$\frac{d\bar{u}_i}{dt} = - \left[\frac{H_{i+1/2}(t) - H_i^+(t)}{\Delta x} + \frac{H_i^-(t) - H_{i-1/2}(t)}{\Delta x} \right], \quad (\text{A.21})$$

where

$$H_{i+1/2} = \frac{f(u_{i+1/2}^+) + f(u_{i+1/2}^-)}{2\phi_{i+1/2}} - \frac{a_{i+1/2}^n}{2} (u_{i+1/2}^+ - u_{i+1/2}^-), \quad (\text{A.22})$$

and

$$H_i^+ = \frac{f(\bar{u}_i)}{\Phi_{i+1/2}}. \quad (\text{A.23})$$

The resulting semi-discrete scheme can then be solved by a SSP Runge–Kutta scheme [44].